Surface and electronic structure at atomic length scales of the nonsymmorphic antiferromagnet $Eu_5In_2Sb_6$

M. Victoria Ale Crivillero,[1] Sahana Rößler,[1] Priscila F. S. Rosa,[2] J. Müller,[3] U. K. Rößler,[4] and S. Wirth[1,*]

[1]*Max Planck Institute for Chemical Physics of Solids, Nöthnitzer Straße 40, 01187 Dresden, Germany*
[2]*Los Alamos National Laboratory, Los Alamos, New Mexico 87545, USA*
[3]*Institute of Physics, Goethe-University Frankfurt, 60438 Frankfurt(M), Germany*
[4]*IFW Dresden, Helmholtzstraße 20, 01069 Dresden, Germany*

(Received 22 March 2022; revised 27 June 2022; accepted 30 June 2022; published 15 July 2022)

We performed scanning tunneling microscopy and spectroscopy (STM/STS) measurements to investigate the Zintl phase $Eu_5In_2Sb_6$, a nonsymmorphic antiferromagnet. The theoretical prediction of a nontrivial Fermi surface topology stabilized by the nonsymmorphic symmetry motivated our research. On the cleaved (010) plane, we obtained striped patterns that can be correlated to the stacking of the $[In_2Sb_6]^{10-}$ double chains along the crystallographic c axis. The attempted cleavage along the a axis revealed a more complex pattern. We combined the STS measurement on nonreconstructed (010) and (081) surfaces with DFT calculations to further elucidate the electronic structure of $Eu_5In_2Sb_6$. From our investigations so far, direct experimental evidence of the predicted topological surface states remains elusive.

DOI: 10.1103/PhysRevB.106.035124

I. INTRODUCTION

Over the past decade, the search for materials with nontrivial electronic band topology has attracted considerable attention [1,2]. The relevance of symmetry considerations has been put in evidence by the discovery of various novel topological phases. Nonsymmorphic space groups, characterized by the nonexistence of an origin that is simultaneously preserved by all symmetries, offers a suitable route to explore new topological electronic materials [3]. Indeed, there are theoretical predictions of nontrivial Fermi surface topology stabilized by the nonsymmorphic symmetry [4].

$Eu_5In_2Sb_6$ crystallizes in a nonsymmorphic orthorhombic structure (space group 55, *Pbam*, lattice parameters $a = 12.510(3)$ Å, $b = 14.584(3)$ Å, $c = 4.6243(9)$ Å [5]). A schematic representation of the crystal structure is presented in Fig. 1(a). This crystal structure is characterized by infinite $[In_2Sb_6]^{10-}$ ribbons oriented parallel to the crystallographic c axis. The ribbons are constituted by two chains of vertex-sharing $InSb_4$ tetrahedra, which are pairwise interconnected by short Sb-Sb bonds, see Fig. 1(b). Noteworthy with respect to the resulting magnetic properties, these polyanionic units are separated by three nonequivalent Eu^{2+} ion sites [5–8]. From the chemical point of view, the crystal structure is an example of a ternary Zintl phase with a precise electron count and, therefore, expected to show insulating behavior. Interestingly, the isostructural compound $Ba_5In_2Sb_6$ (wallpaper group *pgg*) was predicted to host topological surface states on the (001) surface [9]. Very recent band structure calculations suggested a similarly nontrivial topology for the (001) surface of the magnetic analog $Eu_5In_2Sb_6$ [10], a claim that calls for experimental verification.

The inclusion of Eu^{2+} ions into the Zintl phase gives rise to magnetism [8,11]. The particular arrangement of the $4f$ localized moments dictates a complex, presently not fully elucidated, magnetic structure. At low temperatures, two antiferromagnetic transitions ($T_{N1} \approx 14$ K and $T_{N2} \approx 7$ K) have been reported [8]. Notably, $Eu_5In_2Sb_6$ exhibits a negative magnetoresistance (MR) that increases strongly upon decreasing the temperature below about 15 T_{N1} and reaches a colossal MR (CMR) value of -99.999% at 9 T and 15 K, just above T_{N1} [8]. Concomitant with the rapid increase of the MR, an anomalous Hall effect (AHE) is observed as well as a deviation of the susceptibility from a Curie-Weiss-type behavior.

The occurrence of CMR in low-carrier density materials containing Eu^{2+} has been linked to the emergence of quasiparticles called magnetic polarons [12,13]. Indeed, the existence of local inhomogeneities in the electronic density of states at the surface of EuB_6 has recently been seen by scanning tunneling microscopy and spectroscopy (STM/STS) and was interpreted as the localization of charge carriers due to polaron formation [14]. It is, however, important to note that most of these CMR materials, ranging from EuB_6 [15] to manganites [16], exhibit ferromagnetic order. In contrast, $Eu_5In_2Sb_6$ [8,17], along with EuTe [18,19] and $Eu_{14}MnBi_{11}$ [20], are candidates for realizing polarons in an antiferromagnet. We note here that magnetic polarons in antiferromagnets are explored only scarcely, see, e.g., Ref. [21] for a review.

*Steffen.Wirth@cpfs.mpg.de

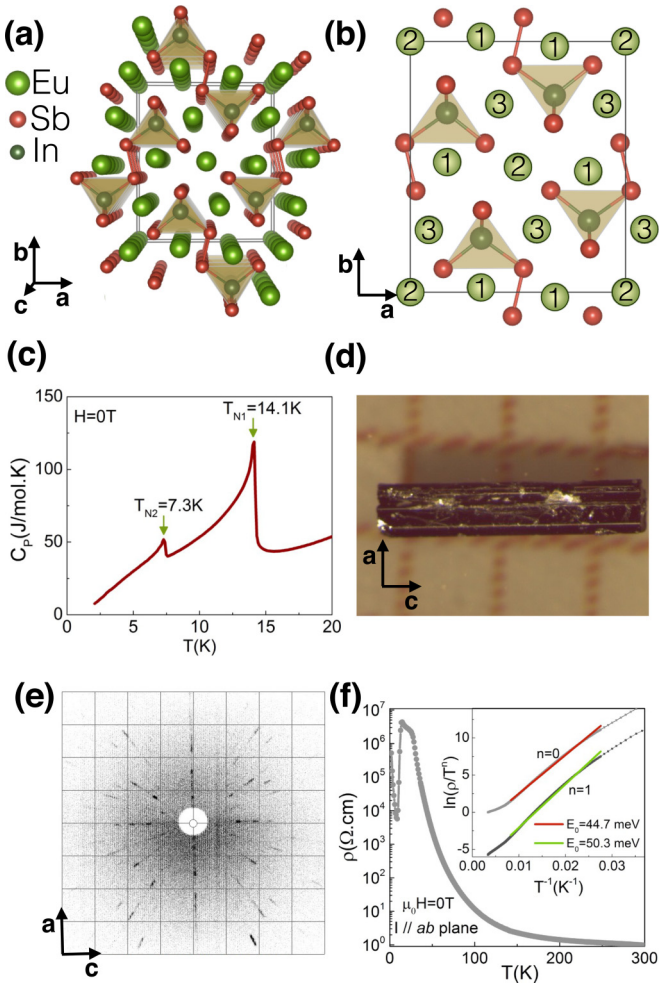

FIG. 1. Crystal structure of $Eu_5In_2Sb_6$: (a) Perspective projections as viewed along the [001] axis and (b) cut along the *ab* plane depicting the three groups of crystallographically unique Eu atoms, Eu(1), Eu(2), and Eu(3), labeled respectively as 1, 2, and 3 for simplicity. (c) Specific heat, C_p, as a function of temperature in zero applied magnetic field. (d) Photograph of an exemplary $Eu_5In_2Sb_6$ single crystal. (e) X-ray Laue patterns along the crystallographic *b* axis. (f) Resistivity $\rho(T)$ as measured in *ab*-plane; inset: estimates of the activation energy (see text).

Here, we report on STM/STS measurements in order to obtained local insights into the electronic structure and surface morphology of the Zintl phase $Eu_5In_2Sb_6$, a nonsymmorphic antiferromagnet. We combine the STS measurements with DFT calculations to further elucidate the density of states (DOS). This work presents a report of the surface structure of an Eu-based ternary Zintl phase.

II. EXPERIMENTAL DETAILS

The single crystals investigated in this work were grown using a combined In-Sb self-flux technique [8]. The rod-like shaped crystals have typical sizes of 0.5 mm × 0.2 mm × 3 mm, with the *c* axis being the long sample axis, see Fig. 1(d). The crystallographic structure was verified by x-ray diffraction using a MWL120 real-time back-reflection Laue camera system. Specific heat measurements were performed using a commercial calorimeter that utilizes a quasiadiabatic thermal relaxation technique.

TABLE I. Details of the $Eu_5In_2Sb_6$ single-crystal surfaces studied by STM/STS.

Sample	#1	#2	#3	#4	#5
Attempted plane	*ac*	*bc*	*ac*	*ab*	*ab*
Assigned plane	(081)	?	*ac*	*ab*	*ab*
Surface quality	many defects	/	extended terraces	atomically rough	

STM/STS was conducted in a commercial low-temperature STM (base temperature ≈4.6 K) under ultrahigh vacuum (UHV) condition, $p \leqslant 3 \times 10^{-9}$ Pa [22], using electrochemically etched tungsten tips. For tunneling spectroscopy, a small ac voltage $V_{\mathrm{mod}} = 0.5$ mV (at a frequency of 117 Hz) was added to the bias voltage V_b and a standard lock-in detection technique was applied. Some of the reported STM data were obtained with a dual-bias mode: two different bias voltages were applied for the forward and backward scans. Therefore, the two topographies were obtained quasisimultaneously under otherwise effectively identical conditions, and specifically within identical areas. If not stated otherwise, the presented STM/STS results were acquired at base temperature. In addition, we also conducted STM/STS measurements at elevated temperatures, 5.9 K $\leqslant T \leqslant$ 17 K, using a resistively heated sample holder. This allowed us to study the temperature evolution of the local density of states (LDOS) across both T_{N1} and T_{N2} at atomically resolved length scales.

We attempted to cleave a total of eight single crystals *in situ* and at low temperatures ($T \approx 20$ K) along the main macroscopic sample axes. As inferred from the diffraction results, those directions are expected to conform with the crystallographic *a*, *b*, and *c* axes. Here we note that knowing the crystallographic sample orientation inside our STM is crucial for a proper assignment of the investigated surface plane below. However, as a result of the subtle anisotropy in the *ab* plane, in some cases further analysis will be needed to unambiguously verify the crystallographic in-plane sample orientation. In Table I details of five surfaces are presented, which were studied in depth. On the remaining samples, atomically flat surface areas were not found.

The electronic structure of $Eu_5In_2Sb_6$ was also examined by calculations using density functional theory (DFT). The calculations were performed using the full-potential local orbital (FPLO) approach [23] as implemented in the FPLO code [24]. We used the generalized gradient approximation (GGA) as exchange-correlation functional [25]. Band structures were also evaluated by fully relativistic calculations in which case the FPLO code includes spin-orbit coupling (SOC) to all orders, being based on solutions of the four-spinor Kohn-Sham-Dirac equations. The magnetic $4f$ configuration of Eu^{2+} is expected to remain in the $L = 0$ and $S = 7/2$ ground state in $Eu_5In_2Sb_6$. Therefore, we applied the open core approach, which places a correspondingly occupied $4f$ shell on the Eu site—in this case an isotropic shell with a net spin of 7/2. This entirely removes the $4f$ levels from the

valence band structure [26–28], while keeping $4f$-$5d$ exchange interactions on site and, thus, allows for indirect exchange couplings via the valence electrons between the Eu-spin moments. Such a fully localized limit for the $4f$ electronic states on Eu^{2+} enabled us to impose various magnetic configurations on the complex crystal structure of $Eu_5In_2Sb_6$ and to estimate their energies in a simplified fashion. Within this method, we explored various collinear spin structures in an effort to examine possible magnetic ground states of $Eu_5In_2Sb_6$. These calculations of different magnetic configurations were conducted within the scalar relativistic approach. We note that the open core treatment of the $4f$ shell constitutes a fully controlled approximation for the behavior of the magnetic Eu^{2+} system within the DFT method. The alternative method by using a DFT+U approach requires an arbitrary parameter that encodes a correlation on the $4f$ shell and can predict a similar electronic structure by shifting the narrow $4f$ bands away from the Fermi energy E_F, but may yield somewhat different results depending on the chosen parametrization.

The calculations of the electronic band structure of $Eu_5In_2Sb_6$ were based on the experimental lattice structure as determined in Ref. [5]. For comparison, we also calculated the electronic band structure for the nonmagnetic analog $Ba_5In_2Sb_6$ for which experimental structure data were taken from Ref. [29].

III. RESULTS

A. Characterization of $Eu_5In_2Sb_6$ single crystals

Figure 1(c) shows the temperature dependence of the specific heat, C_p, in zero magnetic field of a representative $Eu_5In_2Sb_6$ single crystal. The overall behavior and more specifically the two antiferromagnetic transitions at $T_{N1} = 14.1$ K and $T_{N2} = 7.3$ K are in good agreement with those previously reported [8]. The H-T phase diagrams of $Eu_5In_2Sb_6$ along the three main crystallographic axes, constructed using a combination of magnetization and heat capacity measurements, will be reported elsewhere.

Figure 1(e) presents a representative x-ray Laue pattern along the crystallographic b axis. For all the single crystals inspected by x ray the main macroscopic sample axes conform with the crystallographic a, b, and c axes, with the shortest sample side parallel to the b axis.

$Eu_5In_2Sb_6$ has been classified as a narrow-gap semiconductor [5,6,8]. This can be inferred from the bulk resistivity $\rho(T)$, see Fig. 1(f). From fits to $\rho(T) \propto T^n \exp(-E_a/k_BT)$, activation energies E_a between 45–50 meV were estimated (for 36 K $\lesssim T \lesssim$ 120 K) depending on whether an Arrhenius ($n = 0$) or small polaron hopping conduction mechanism ($n = 1$) [30] was assumed [inset to Fig. 1(f)]. These values of E_a are in excellent agreement with those of Ref. [8] while much larger values were reported in Ref. [6].

B. STM: Topography

Interestingly, we found stable tunneling conditions only using relatively large bias voltages V_b. In Fig. 2 an overview of different atomically flat surfaces encountered on samples #1 and #2 is presented ($V_b = +2$ V). These samples were attempted to be cleaved along the nominal a axis, i.e., the bc plane is expected to be exposed. In general, this kind of topography has to be searched for; as mentioned above, on some cleaved sample surfaces we did not succeed to find atomically flat areas at all. One principal axis can easily be identified in most cases, the orientation of which corresponds to the crystallographic c axis. The types of observed topographies ranges from more disordered ones, Fig. 2(a), to almost defect-free surfaces with step edges, Fig. 2(d). Clearly, the diversity of observed topographies puts in evidence that $Eu_5In_2Sb_6$ surfaces are prone to manifest complex configurations, which reinforces the relevance of studying the surface properties with a local probe as STM/STS.

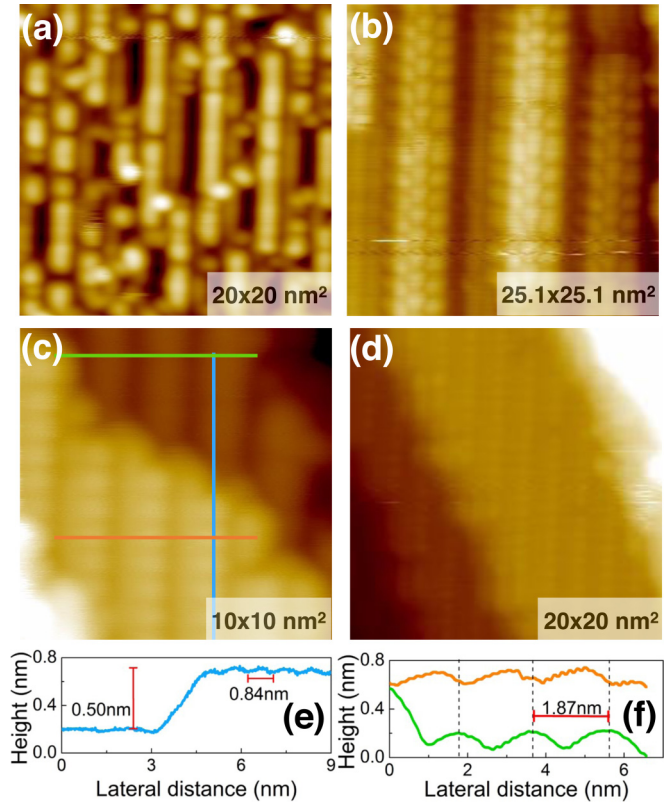

FIG. 2. Overview of different topographies encountered on $Eu_5In_2Sb_6$ cleaved surfaces ($V_b = +2$ V and current set point $I_{sp} = 1.4$ nA). (a), (b), and (d): Three different areas on sample #2, $T = 4.6$ K. (c) Topography on sample #1 at $T = 5.9$ K and, (e), (f) height profiles along the lines marked by similar colors in (c).

The two representative topographies in Figs. 2(c) and 2(d) exhibit atomically flat areas separated by subnanometer-high step edges. They were observed on two different samples, #1 and #2, over areas of 10×10 nm^2 and 20×20 nm^2, respectively. The average height of the step edges is 0.50 nm, as seen from the line scan in Fig. 2(e) taken along the turquoise line in Fig. 2(e). The distance between corrugations along the c axis in the upper plane is about 0.84 nm. Noticeably, there is a displacement between the corrugations within the two adjacent planes; compare, for example, the orange and green line scans in Fig. 2(f). In this case, the distances between corrugations ($\Delta x \approx 1.87$ nm, $\Delta y \approx 0.84$ nm) and the step height $\Delta z \approx 0.50$ nm did not match with the expected values

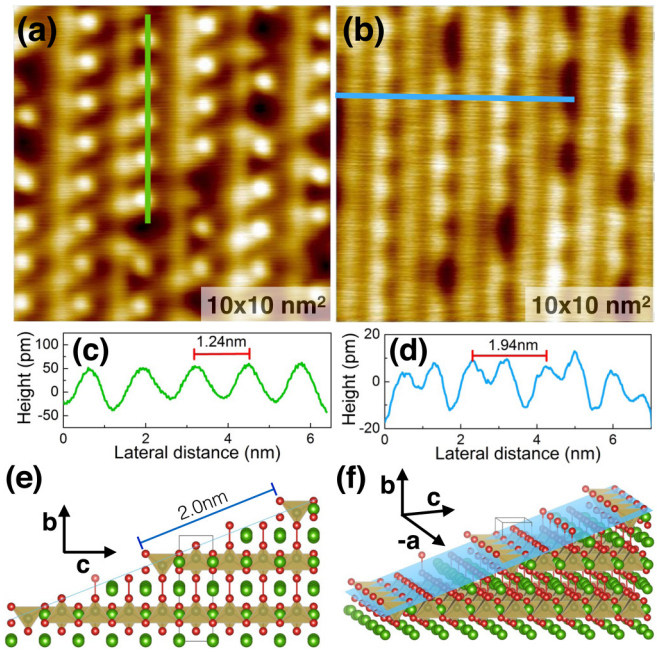

FIG. 3. STM topography of an atomically flat area of 10×10 nm^2 on sample #1, obtained in dual-bias mode at $T = 5.9$ K and $I_{sp} = 1.4$ nA. (a) $V_b = +2$ V; (b) $V_b = -2$ V. (c) and (d) Height profiles along the marked lines in (a) and (b), respectively. (e) Schematic representation of a proposed surface termination cleaved along the plane (081). Here, the horizontal separation $\Delta x = 2.0$ nm between the stripes is marked. (f) Perspective view: the exposed tetrahedra constituting the stripes along the a axis are separated by 1.25 nm, in agreement with the measurement in (c).

for a nonreconstructed bc plane, i.e., this likely represents a reconstructed surface.

On sample #1, a different type of atomically flat pattern could be observed, see Fig. 3. Again, the topographies in Figs. 3(a) and 3(b) were obtained in dual-bias mode, i.e., with $V_b = +2$ V and -2 V, respectively. In this case, the double-stripe-like corrugations are separated by $\Delta y \approx 1.94$ nm, while the distance of corrugations along the stripe direction is $\Delta x \approx 1.24$ nm. The closeness of the latter distance to the lattice parameter a suggests that the cleaved surface may contain the crystallographic a axis. To further identify the surface plane, we searched in the crystal structure for planes with an orientation close to ac and which contain features separated by 1.94 nm. A suitable candidate is the (081) plane; see the schematic representations in Figs. 3(e) and 3(f). In that case, the distance between the exposed tetrahedra along the a axis is a, while the horizontal separation between the so-formed stripes is 2.00 nm. The tilting angle between the (081) plane and the ac plane is 22°. Noticeably, some crystals exhibit facets at ∼30° from the a axis. Therefore, a plausible scenario is that this sample was mounted parallel to one of those facets before cleaving such that the crystal was then cleaved along the (081) plane. Regarding the topographies Figs. 3(a) and 3(b), it is worth noting three observations. First, there is a noticeable difference in contrast for the two V_b values applied (see also Fig. 4) suggesting a complex energy and spatial dependence of the types of states dominating the tunnel current. Second, this type of pattern extends over relatively large areas without step edges. Third, there is an appreciable number of defects observed.

To gain further insight into the dependence of the contrast in topography on V_b, a series of five images of the same area was taken in dual-bias mode (positive and negative V_b) with $|V_b|$ increasing from 1–4 V, see Fig. 4. Note that these images were obtained on the same cleave and close to the area shown in Figs. 3(a) and 3(b). While the contrast is strongly enhanced for positive V_b, there is no contrast reversal or lateral shift of corrugations observed upon reversing V_b, neither for the regular features nor for the defects. These observations are consistent with an above-indicated assignment of the regularly arranged protrusions to negatively charged Sb in either the $InSb_4$ tetrahedra or the short Sb-Sb bonds between them,

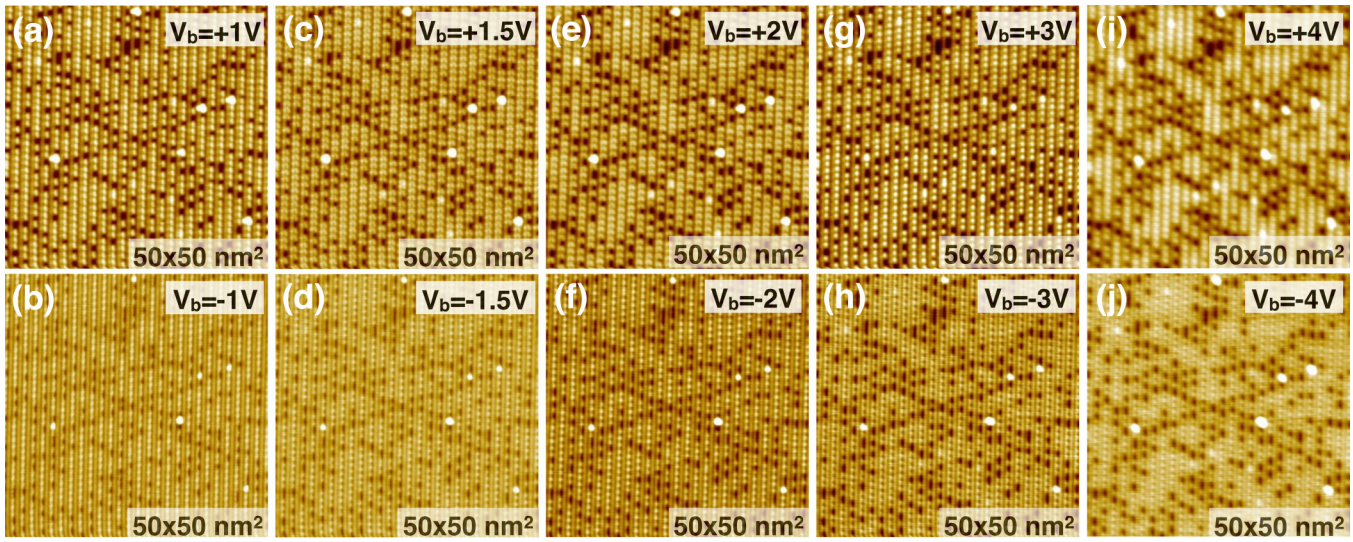

FIG. 4. STM topographies obtained in dual-bias mode on a relatively big identical area of 50×50 nm^2 on sample #1 ($I_{sp} = 1.4$ nA, $T = 5.9$ K). Images obtained within the same run are stacked on top of each other and with V_b indicated. The color codes of all shown topographies correspond to a total height scale of approximately 300 pm from black to white.

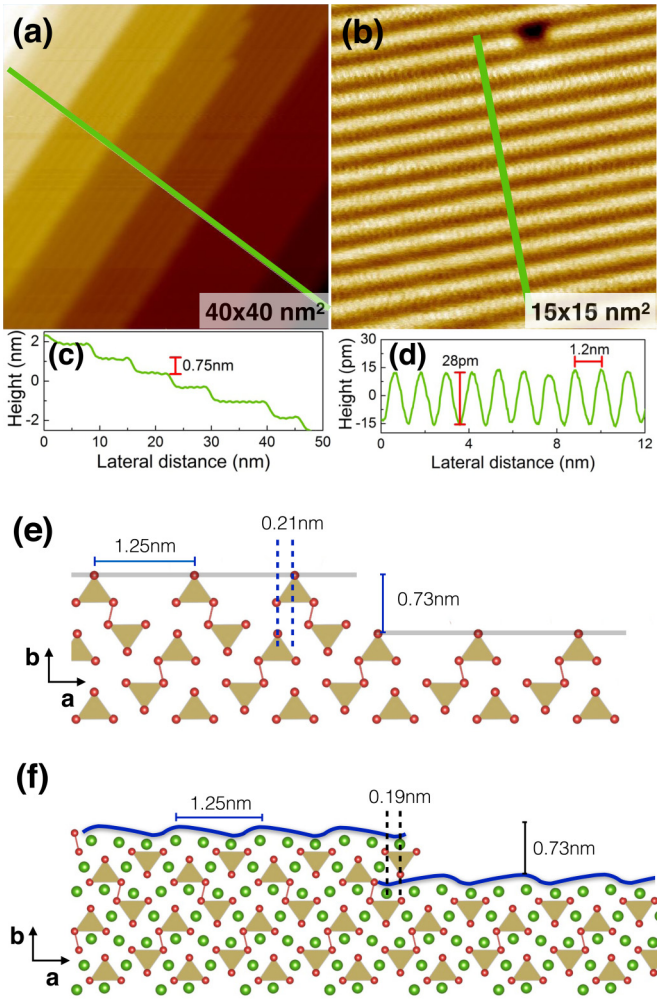

FIG. 5. Topography of nonreconstructed, atomically flat surfaces cleaved along the *ac* plane (sample #3). (a) and (b) STM topographies obtained with $V_b = -3$ V and $I_{sp} = 1.4$ nA at $T = 7.0$ K and $T = 5.9$ K, respectively. (c) and (d) Height profiles along the corresponding lines marked in (a) and (b). (e) Schematic representation of the proposed Sb-terminated surface cleaved along the *ac* plane and a corresponding subunit cell terrace. Note that for simplicity only the tetrahedra are shown. Their double-chain stacking imposes a lateral spacing of the protrusions of $a = 1.25$ nm along the a axis and a vertical distance to the next Sb-terminated surface $\frac{1}{2}b = 0.73$ nm. (f) Alternative Eu-terminated (010) plane formed by breaking the short Sb-Sb bonds during the cleaving. The resulting height-modulated surface also exhibits a 1.25 nm period along a and 0.73 nm step edges along b.

cf. Figs. 3(e) and 3(f). However, to fully interpret the STM topographies, a comparison with simulated STM images will be required [31,32].

Motivated by the results presented above, the following sample #3 was attempted to be cleaved along the *ac* plane. Here, we were able to locate some areas where the in-plane arrangement of corrugations and the height of step edges match the values expected for an *ac* surface. In Fig. 5 we present a striped pattern with a lateral spacing of 1.2 nm, while the height difference between terraces is 0.75 nm $\approx \frac{1}{2}b$. Notably, the density of defects, apart from the step edges, is very low. Before attempting to correlate this arrangement with a certain surface termination, we emphasize that the crystallographic orientation of the sample is known from prior Laue measurements. The striped pattern may then be assigned to the double-chain stacking, where each stripe corresponds to the end part of the chains, see Fig. 5(e), constituting a Sb-terminated surface. An alternative scenario arises by considering the surface composed by the Eu(1) and Eu(2) ions and formed by breaking the short Sb–Sb bonds during the cleaving process, cf. Fig. 5(f), again forming a height-modulated surface with periodicity a and possible step edges of $\frac{1}{2}b$. On both types of terminations, there is an in-plane displacement between the corrugations on both sides of a step edge, cf. Figs. 5(e) and 5(f); the expected value in the Sb-terminated scenario is 0.21 nm and for the Eu-terminated one 0.19 nm. Unfortunately, the small difference between the values and the lack of atomic resolution along the c axis renders an identification of the surface termination challenging. Nonetheless, the small difference of the Eu(1) positions along b direction and the expected asymmetry of the stripes along a make an Eu-terminated surface less likely. Also from an energetic point of view, an Eu-terminated surface appears unfavorable considering the involved Sb_2-Sb_2 bond breaking. Yet, further surface energy calculations are needed to assess the surface termination. In addition, due to the lack of atomic resolution in Fig. 5(b) a surface reconstruction cannot be ruled out completely.

Finally, motivated by the predictions of topological surface states on the (001) surface of $Ba_5In_2Sb_6$ [9], we attempted to cleave samples #4 and #5 along the c axis. Unfortunately and despite exhaustive efforts, atomically flat surface areas could not be found. Intuitively, the experimental absence of ordered flat surfaces may be understood by considering that the breaking of the double chains is very likely unfavorable.

C. STS

STS has evolved into a widespread tool mainly because the local tunneling conductance $g(V,T) = dI(V)/dV$ is, within simplifying approximations, proportional to the local DOS. Consequently, measurements of $g(V,T)$ can provide insight into the local electronic structure and its temperature evolution at the sample surface [33].

An overview of the local conductance, $g(V,T) = dI(V)/dV$, as measured by STS on $Eu_5In_2Sb_6$, is presented in Fig. 6. A comparison of the results obtained on two atomically flat surfaces at 5.9 K is presented in Fig. 6(a): the nonreconstructed *ac* surface of sample #3, here called S1, and the (081) plane of sample #1, denoted S2. In both cases, $g(V)$ spans several orders of magnitude (note the logarithmic scale) within the range -2 V $\leqslant V_b \leqslant +2$ V with deep, yet finite minima. This finding is in good agreement with the large resistivity values at low temperature, see Fig. 1(f). Beyond this, there are clear differences between S1 and S2: (i) $g(V)$ is significantly higher on S2, specifically for $V_b \leqslant 0$. (ii) While the minimum of $g(V)$ is very close to $V_b = 0$ for S1, it appears to be shifted to $V_b \approx 260$ mV. (iii) the gap width appears to be slightly smaller on S2. Likely, these observations result from the more disturbed surface with larger defect density of S2, given the insulating behavior of $Eu_5In_2Sb_6$ at this low

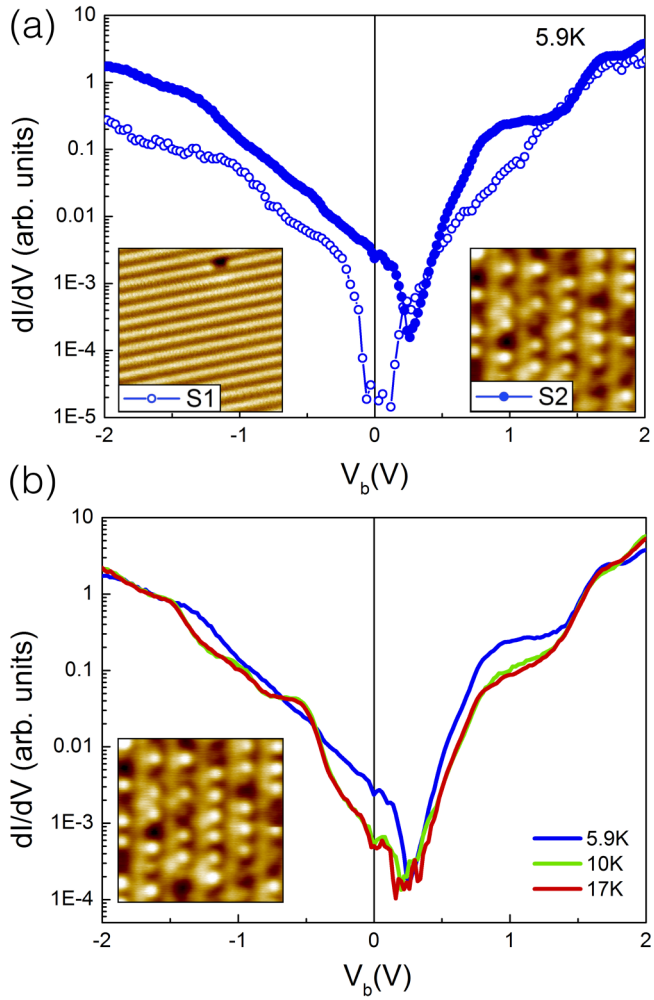

FIG. 6. (a) Averaged spectra taken at 5.9 K on two atomically flat surfaces of $Eu_5In_2Sb_6$: the nonreconstructed *ac* plane, S1, and the (081) plane, S2. The insets present the corresponding topographies, cf. Figs. 5(b) and 3(a). (b) T dependence of dI/dV spectra on S2 covering temperatures below, in between and above T_{N1} and T_{N2}.

temperature. However, it should be emphasized that the measured $g(V)$ values remain finite within the pseudogap even for the well-ordered surface S1.

The temperature dependence of $g(V, T)$ was studied on surface S2, see Fig. 6(b). In particular, we repeated the measurements below and above T_{N1} and T_{N2} several times in order to evaluate any possible influence of the antiferromagnetic order on $g(V, T)$. At all temperatures, the minimum of $g(V, T)$ is found at positive V_b. In general, there is no significant difference between the spectra taken at 10 K and 17 K, i.e., around $T_{N1} = 14.1$ K. In contrast, below $T_{N2} = 7.3$ K [see spectrum at $T = 5.9$ K in Fig. 6(b)] the conductance at $V_b = 0$, and therefore the LDOS at E_F, is increased by almost one order of magnitude.

D. Density functional theory calculation

In order to calculate the DOS of the ground state using DFT, it is necessary to first determine the ground-state magnetic configuration. In consequence, we start by describing the calculation of energies for the different magnetic configurations, and subsequently, calculate the DOS of the energetically most favorable configurations.

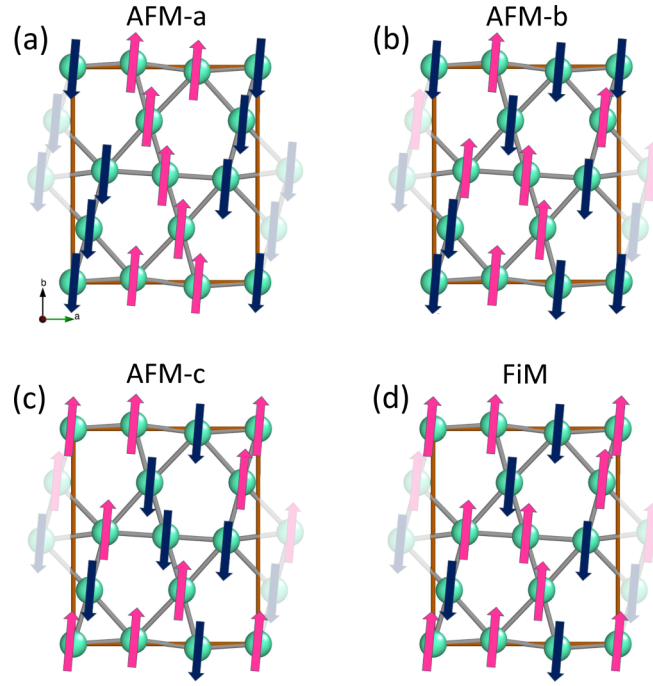

FIG. 7. Magnetic configurations of lowest energy according to DFT calculations: (a)–(c) Fully compensated antiferromagnetic (AFM) states from collinear DFT (spin resolved). (d) First ferrimagnetic (FiM) configuration. The crystallographic orientation conforms to the one in Fig. 1(b).

1. Magnetic configurations

$Eu_5In_2Sb_6$ contains ten Eu ions in the *ab* base plane of the unit cell. These sites belong to three different Wyckoff positions of the space group *Pbam*; Eu(1) and Eu(3) both occupy two different sets of 4*g* sites and Eu(2) the 2*a* sites. In order to probe possible magnetic configurations, we have conducted DFT calculations for all combined magnetic states that can be created from either fully saturated ferromagnetic (FM) or fully compensated antiferromagnetic (AFM) collinear spin configurations of these three magnetic subsystems, amounting to 128 magnetic configurations. The calculations were executed with the scalar relativistic DFT approach and using the open-core method. The four configurations with lowest calculated energies are sketched in Fig. 7. The corresponding energies with respect to the AFM-a state and the magnetic spin moments are listed in Table II. The A-type configuration has ferromagnetically coupled Eu spin moments in the *ab* plane, which are alternatingly stacked in an antiparallel staggered order. Such a spin structure has been proposed as possible magnetic order in Ref. [8].

In addition, for the antiferromagnetic configurations with lowest energies, fully relativistic calculations were conducted. The corresponding results suggest that: (i) The effective coupling between the Eu layers likely is ferromagnetic. (ii) There are strong antiferromagnetic couplings within the *ab* plane between Eu ions within the three sublattices of Eu(1), Eu(2),

TABLE II. Results of total energies calculated by DFT for different spin configurations in $Eu_5In_2Sb_6$ and the spin moments on the Eu sites of the three different sublattices. The spin configurations FM, FiM, and AFM represent ferromagnetic, ferrimagnetic, and antiferromagnetic ones, respectively, as illustrated in Fig. 7 (except FM).

Name	Configuration	Magnetic spin moments			Energy
	lattice sites (Eu(1))(Eu(2))(Eu(3))	$\lvert m_s^{(1)}\rvert$	$\lvert m_s^{(2)}\rvert$ [μ_B/Eu]	$\lvert m_s^{(3)}\rvert$	relative to AFM-a [meV/unit cell]
FM	(↑↑↑↑)(↑↑)(↑↑↑↑)	7.154	7.169	7.160	87.600
FiM	(↑↓↑↓)(↑↑)(↑↓↑↓)	7.200	7.189	7.203	2.164
AFM-c	(↑↓↑↓)(↑↓)(↑↓↑↓)	7.202	7.201	7.211	0.055
AFM-b	(↑↓↑↓)(↓↑)(↑↓↑↓)	7.209	7.201	7.206	0.055
AFM-a	(↑↑↓↓)(↓↑)(↓↓↑↑)	7.179	7.210	7.212	0

and Eu(3) sites. (iii) The close match of energies for the different AFM and the ferrimagnetic configuration indicates that this multisublattice spin system is likely frustrated. The reason is presumably geometric frustration related to triangular and pentagonal elementary plaquettes between nearest-neighbor Eu sites. In consequence, the correct magnetic ground state of $Eu_5In_2Sb_6$ is likely a complex noncollinear AFM or ferrimagnetic state to lift this frustration. However, magnetic couplings beyond next neighbors may also play a role. Since the $4f$ electrons of Eu^{2+} are tightly bound to the Eu-ion cores, the magnetic exchange mechanism between the Eu is indirect, likely of the Ruderman-Kittel-Kasuya-Yosida (RKKY)-type, which can support long-range contributions, both in plane and out of plane. Our restricted computational results do not allow a complete computational determination of the magnetic ground state, which includes these intricacies.

It is noteworthy that the lowest-energy magnetic configurations do not break inversion symmetry and, if no cell doubling is enforced by these long-range couplings, the system of magnetic Γ-point modes calculated is complete in the so-called exchange approximation. If the magnetic ground state of $Eu_5In_2Sb_6$ is described by a suitable combination of such Γ-point modes, a relatively simple spin structure with compensated moments may approximately describe this magnetic system. However, in that case spin-orbit coupling (SOC) does allow for the occurrence of weak ferromagnetism by spin canting in this orthorhombic magnetic crystal [34], as the Dzyaloshinskii-Moriya exchange is allowed. In fact, experimental data on $Eu_5In_2Sb_6$ revealed a very small in-plane ferromagnetic component and hysteresis, which was ascribed to the complex magnetic structure with canted moments [8]. As such, the intrinsic weak ferromagnetism may be linked to the primary AFM Γ-point order.

Sizeable effects by SOC are seen in the results of fully relativistic (fr) calculations with different quantization axes in Table II. From an experimental point of view, a determination of the magnetic ground state and a detailed understanding of the magnetic field–temperature phase diagram for $Eu_5In_2Sb_6$ will require major efforts. Our theoretical results, however, suggest that the basic spin structure is antiferromagnetic within the *ab* plane. A simple A-type antiferromagnetic structure appears unlikely. Nonetheless, the evaluation of the electronic band structure below is based on the collinear low-energy spin structures (Fig. 7), which are expected to approximate the essential features of ordered magnetism in $Eu_5In_2Sb_6$.

The fully relativistic calculations may yield some estimates about the relevance and even magnitudes of magnetic anisotropies. Yet, for the collinear configurations only effective anisotropies can be determined for the orthorhombic lattice of $Eu_5In_2Sb_6$. The easy, intermediate, and hard axes are aligned parallel to the main crystallographic axes, owing to the *mmm* symmetry. For the three different configurations, AFM-a, AFM-b, and FM (see Table II and Fig. 7), we find in all cases the easy, intermediate and hard axis along the *b*, *a*, and *c* direction, respectively. We note that the numerical estimates for the effective anisotropies [defined as difference between total energies for spins in hard (intermediate) and easy axis orientation] are 0.8 (0.3) meV/(unit cell) in AFM-a configuration. For the AFM-b and FM configurations, these anisotropies are 1.6 (1.1) meV/(unit cell) and 1.7 (0.6) meV/(unit cell), respectively. These anisotropies are substantially large, and there is an essential dependence of these anisotropies on the magnetic state. This is the expected behavior, as the Eu^{2+} state with orbital angular momentum $L = 0$ does not carry a single-ion anisotropy. Consequently, the anisotropies are determined by the anisotropic exchange between the Eu sites. Moreover, the low symmetry of the different Eu lattice sites [Fig. 1(a)] implies that Dzyaloshinskii-Moriya interactions (DMIs) due to the absence of inversion symmetry and conventional exchange interactions are allowed on almost all bonds. Formally, the DMIs result from a first-order effect of the spin-orbit coupling and can become large. Therefore, the effective anisotropies are the result of sums and differences between these anisotropic exchange interactions, which act in addition to the geometric frustration inherent in the Eu-sublattice structure of $Eu_5In_2Sb_6$, and may cause canted spin structures. The experimentally found indications of a weak ferromagnetic moment [8] may find an explanation in the existence of such large DMIs. However, a noncollinear ferrimagnetic ground state caused by the geometric frustration may also play a role in such multisublatttice magnetic structure. Here, a detailed experimental resolution of the spin structure in $Eu_5In_2Sb_6$ would be desirable.

2. Electronic band structure

In an effort to gain further insight into the band structure of $Eu_5In_2Sb_6$ and to allow for comparison to our STS results (Fig. 6), the electronic density of states (DOS) for both the ferromagnetic (FM) and the AFM spin configuration AFM-a

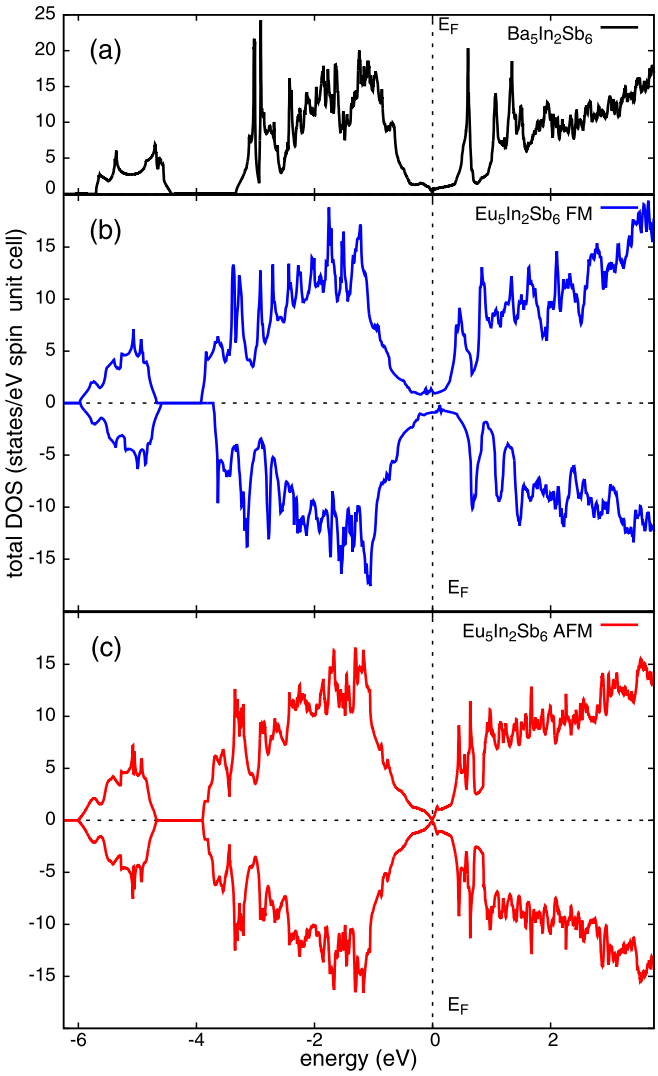

FIG. 8. Density of states (DOS) from scalar relativistic (sr) DFT calculations: (a) $Ba_5In_2Sb_6$, (b) $Eu_5In_2Sb_6$ in the ferromagnetic (FM) state. (c) $Eu_5In_2Sb_6$ in antiferromagnetic state, AFM-a configuration.

with lowest energy were calculated, see Fig. 8. In addition, the DOS of the nonmagnetic isostructural compound $Ba_5In_2Sb_6$ is shown. All three systems behave as semimetals with a small DOS near E_F. Qualitatively, the gaplike features observed for $Eu_5In_2Sb_6$ in both the calculations and the STS data even share the asymmetry of a somewhat steeper rise for positive energies compared to the negative side.

A closer inspection of the energy region near E_F (Fig. 9) reveals a significant difference between the FM and the AFM configuration. The AFM state with compensated total moments has a significant depression of the DOS right at E_F compared to the FM state. These results for the AFM state are also in line with the STS data discussed above. The comparison of fully relativistic (fr) and scalar relativistic band structure calculations near E_F also shows a remarkable redistribution and more structured DOS for the former, but it does not change the overall picture.

In an effort to gain insight into a possible nontrivial electronic band topology of $Eu_5In_2Sb_6$, the momentum-resolved band structure as obtained by a scalar relativistic DFT

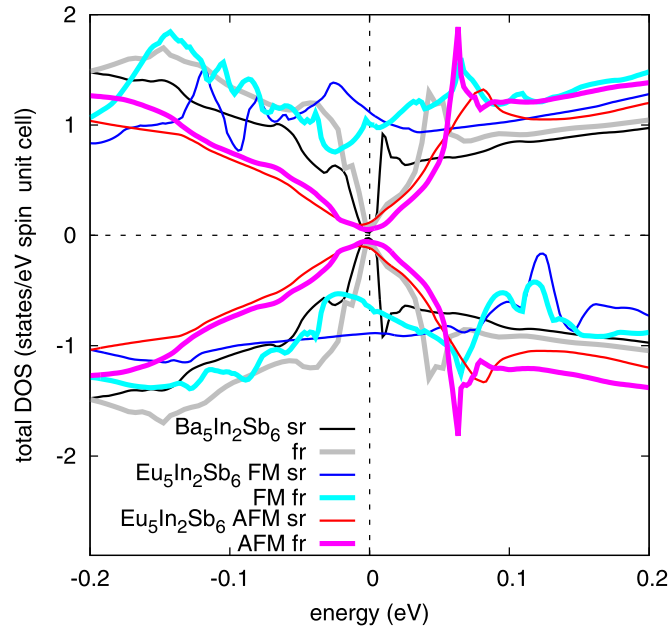

FIG. 9. DOS near the Fermi energy E_F (at zero energy). A comparison between fully relativistic (fr) and scalar relativistic (sr) DFT calculations for $Eu_5In_2Sb_6$ in FM and AFM spin configuration as well as $Ba_5In_2Sb_6$ is shown.

calculation for AFM-a configuration is presented in Fig. 10. Clearly, there are certain spin-split bands crossing E_F in the AFM state, see section along X-S-Y in the energy-enlarged inset. These results are in good agreement with those obtained by other band structure calculations [10]. It should be noted, however, that care has to be taken when comparing results of different calculation schemes: On the one hand, the magnetism of $Eu_5In_2Sb_6$ is included in our calculations. On the other hand, SOC is only considered in the fully relativistic calculations presented in Fig. 9 while it is neglected in the scalar relativistic ones. Our calculations do not provide any

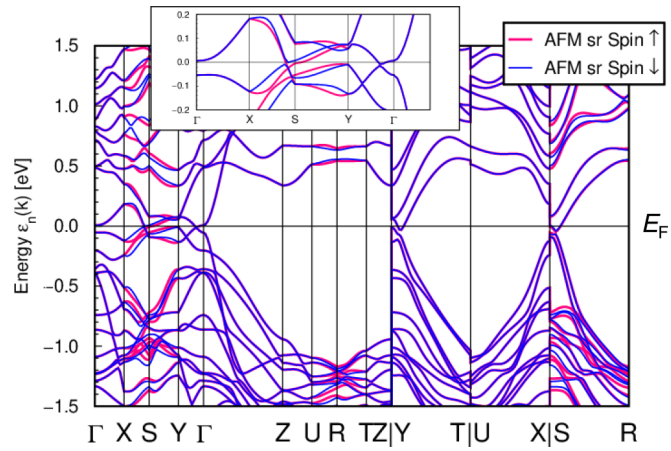

FIG. 10. Band structure of $Eu_5In_2Sb_6$ in the AFM-a spin configuration. The insets show details near the Fermi energy E_F, which is set to zero energy. The scalar-relativistic DFT calculations are represented by spin-split band data for spin majority and minority components.

indication for a nontrivial band topology, in line with a trivial $\mathbb{Z}_2$ index proposed in Ref. [35]. This is consistent with our STS data, at least for the surfaces investigated so far. Nonetheless, to scrutinize the surface topology in $Eu_5In_2Sb_6$, the topological invariants for the double-glide (001) surface should be explored by Wilson loop calculations, similar to those for $Ba_5In_2Sb_6$ in Ref. [9].

IV. DISCUSSION AND CONCLUSIONS

$Eu_5In_2Sb_6$ was successfully cleaved *in situ* and patches of atomically flat areas, specifically for the *ac* surface plane, were located. Within such areas, our STS data indicated gaplike spectra with a very low, but finite conductance at the Fermi level. Qualitatively, the STS data agree with the calculated DOS in the energy range from -1 to $+1$ eV. The calculated band structures and resultant DOS for the AFM and FM spin structures in $Eu_5In_2Sb_6$ ultimately illustrate how the difference in spin configuration can lead to a reorganization of the small band contributions near E_F. Apart from such subtlety, the major influence of the underlying Eu $4f$ spin structure suggests a rather traditional picture for the electronic properties of this compound. In the AFM state, the material has only rather few charge carriers available, and the AFM background allows only for incoherent hopping transport via thermal activation. The former result is in good agreement with the very small but finite local DOS near E_F observed by STS, while the latter may lead to an effective insulatorlike behavior as indeed observed in the resistivity measurements. In particular, a negative temperature coefficient of the resistivity, $d\rho/dT < 0$, may be caused by the stiffening of the AFM correlations upon lowering the temperature above, and even through, the magnetic phase transitions. For decreasing temperature and/or under applied magnetic field, spin polarons can be formed and may lead to strongly improved conduction, resulting in a CMR behavior. The enhanced DOS in the FM state shows [see Fig. 8(b)], how such a spin-polarized electronic structure generates charge carriers.

The DFT-band structure for the different magnetic solutions all show semimetallic behavior, in agreement with comparable calculations reported in Ref. [35]. In this work by Varnava *et al.*, it was shown that insulating or semimetallic band structures can be close to each other for the whole class of $Eu_5In_2X_6$ materials, as they can be tuned by certain lattice distortions in the nonmagnetic case. The role of spin splitting and spin-orbit coupling, however, is not clear at the moment. A comparison between the theoretical band structure and the macroscopic transport data for $Eu_5In_2Sb_6$ (the latter of which finds insulating properties) is not straightforward. The DFT method within our approach is known to yield incorrect magnitudes for band gaps in semiconductors, such that the small indirect band gap of 40 meV estimated from resistivity data of $Eu_5In_2Sb_6$ [8] may be missed. In addition, the formation of magnetic polarons and the corresponding inhomogeneous magnetic state [8,17] may further complicate a comparison between theoretical and experimental results. Clearly, the question regarding the detailed band structure of $Eu_5In_2Sb_6$ in close vicinity (on the meV scale) of E_F and its dependence on the magnetic state requires further attention.

At present, neither our band structure calculations for the AFM-a state nor the STS results at low temperature provide any indication for a nontrivial band topology of $Eu_5In_2Sb_6$. Nonetheless, our future experimental efforts will focus on an optimization of cleaved (001) surfaces as atomically flat surfaces of this orientation appear to be essential for conclusive results concerning the topological nature of $Eu_5In_2Sb_6$.

ACKNOWLEDGMENTS

We thank U. Nitzsche for technical assistance with respect to the DFT calculations and U. Schwarz for insightful discussions. Work at Los Alamos was supported by the Los Alamos Laboratory Directed Research and Development program through Project No. 20220135DR. S.R. acknowledges support by the Deutsche Forschungsgemeinschaft (DFG, German Research Foundation) through SFB 1143. Work at the Max-Planck-Institute for Chemical Physics of Solids in Dresden and at Goethe University Frankfurt was funded by the Deutsche Forschungsgemeinschaft (DFG, German Research Foundation), Project No. 449866704.

[1] T. Zhang, Y. Jiang, Z. Song, H. Huang, Y. He, Z. Fang, H. Weng, and C. Fang, Nature (London) **566**, 475 (2019).
[2] F. Tang, H. C. Po, A. Vishwanath, and X. Wan, Nature (London) **566**, 486 (2019).
[3] Z. Wang, A. Alexandradinata, R. J. Cava, and B. A. Bernevig, Nature (London) **532**, 189 (2016).
[4] S. A. Parameswaran, A. M. Turner, D. P. Arovas, and A. Vishwanath, Nature Phys. **9**, 299 (2013).
[5] S.-M. Park, E. S. Choi, W. Kang, and S.-J. Kim, J. Mater. Chem. **12**, 1839 (2002).
[6] S. Chanakian, U. Aydemir, A. Zevalkink, Z. M. Gibbs, J.-P. Fleurial, S. Bux, and G. J. Snyder, J. Mater. Chem. C **3**, 10518 (2015).
[7] M. Radzieowski, F. Stegemann, S. Klenner, Y. Zhang, B. P. T. Fokwa, and O. Janka, Mater. Chem. Front. **4**, 1231 (2020).
[8] P. F. S. Rosa, Y. Xu, M. Rahn, J. Souza, S. Kushwaha, L. Veiga, A. Bombardi, S. Thomas, M. Janoschek, E. Bauer *et al.*, npj Quantum Mater. **5**, 52 (2020).
[9] B. J. Wieder, B. Bradlyn, Z. Wang, J. Cano, Y. Kim, H.-S. D. Kim, A. M. Rappe, C. L. Kane, and B. A. Bernevig, Science **361**, 246 (2018).
[10] Y. Xu (private communication).
[11] U. Subbarao, S. Sarkar, B. Joseph, and S. C. Peter, J. Alloys Compd. **658**, 395 (2016).
[12] T. Kasuya and A. Yanase, Rev. Mod. Phys. **40**, 684 (1968).
[13] S. von Molnár, Sens. Actuators, A **91**, 161 (2001).
[14] M. Pohlit, S. Rößler, Y. Ohno, H. Ohno, S. von Molnár, Z. Fisk, J. Müller, and S. Wirth, Phys. Rev. Lett. **120**, 257201 (2018).
[15] S. Süllow, I. Prasad, S. Bogdanovich, M. C. Aronson, J. L. Sarrao, and Z. Fisk, J. Appl. Phys. **87**, 5591 (2000).
[16] M. B. Salamon and M. Jaime, Rev. Mod. Phys. **73**, 583 (2001).

[17] J. C. Souza, S. M. Thomas, E. D. Bauer, J. D. Thompson, F. Ronning, P. G. Pagliuso, and P. F. S. Rosa, Phys. Rev. B **105**, 035135 (2022).
[18] N. F. Oliveira, Jr., S. Foner, Y. Shapira, and T. B. Reed, Phys. Rev. B **5**, 2634 (1972).
[19] Y. Shapira, S. Foner, N. F. Oliveira, Jr., and T. B. Reed, Phys. Rev. B **5**, 2647 (1972).
[20] J. Y. Chan, S. M. Kauzlarich, P. Klavins, R. N. Shelton, and D. J. Webb, Phys. Rev. B **57**, R8103 (1998).
[21] S. von Molnár and P. A. Stampe, in *Handbook of Magnetism and Advanced Magnetic Materials*, edited by H. Kronmüller and S. Parkin (John Wiley & Sons, New York, 2007), Vol. 5, pp. 2689–2702.
[22] Scienta Omicron GmbH, Taunusstein (Germany).
[23] K. Koepernik and H. Eschrig, Phys. Rev. B **59**, 1743 (1999).
[24] Calculations have been performed using fplo18.00., https://www.fplo.de.
[25] J. P. Perdew, K. Burke, and M. Ernzerhof, Phys. Rev. Lett. **77**, 3865 (1996).
[26] M. S. S. Brooks, L. Nordström, and B. Johansson, J. Phys.: Condens. Matter **3**, 3393 (1991).
[27] M. S. S. Brooks, L. Nordström, and B. Johansson, J. Phys.: Condens. Matter **3**, 2357 (1991).
[28] M. Richter, J. Phys. D: Appl. Phys. **31**, 1017 (1998).
[29] G. Cordier and M. Stelter, Z. Naturforsch. B **43**, 463 (1988).
[30] D. Emin and T. Holstein, Ann. Phys. (NY) **53**, 439 (1969).
[31] H. Mönig, M. Todorović, M. Z. Baykara, T. C. Schwendemann, L. Rodrigo, E. I. Altman, R. Pérez, and U. D. Schwarz, ACS Nano **7**, 10233 (2013).
[32] T. Woolcot, G. Teobaldi, C. L. Pang, N. S. Beglitis, A. J. Fisher, W. A. Hofer, and G. Thornton, Phys. Rev. Lett. **109**, 156105 (2012).
[33] J. Tersoff and D. R. Hamann, Phys. Rev. B **31**, 805 (1985).
[34] A. N. Bogdanov, U. K. Rößler, M. Wolf, and K. H. Müller, Phys. Rev. B **66**, 214410 (2002).
[35] N. Varnava, T. Berry, T. M. McQueen, and D. Vanderbilt, Phys. Rev. B **105**, 235128 (2022).